Chemical Engineering Journal 425 (2021) 130566

Contents lists available at ScienceDirect

Chemical Engineering Journal

journal homepage: www.elsevier.com/locate/cej

# Enhanced fire safety and mechanical properties of epoxy resin composites based on submicrometer-sized rod-structured methyl macrocyclic silsesquioxane sodium salt

Xinming Ye [a,b], Jingjing Li [a], Wenchao Zhang [a,*], Ye-Tang Pan [a], Rongjie Yang [a,*], Jiarong Li [b]

[a] National Engineering Technology Research Center of Flame Retardant Material, School of Materials, Beijing Institute of Technology, 5 South Zhongguancun Street, Haidian District, Beijing 100081, PR China
[b] School of Chemistry and Chemical Engineering, Beijing Institute of Technology, 5 South Zhongguancun Street, Haidian District, Beijing 100081, PR China

ARTICLE INFO

*Keywords:*
Macrocyclic silsesquioxanes
Epoxy resin
Flame retardancy
Smoke suppression
Mechanical property

ABSTRACT

Facile synthesis of multifunctional macromolecules endowed with low cost has always been a considerable challenge for chemists. Herein, a series of methyl macrocyclic oligomeric silsesquioxane sodium salt (Na-MOSS) were synthesized via the simplified one-pot method. FTIR, NMR, MALDI-TOF MS and XRD results suggested that Na-MOSS endowed with well-defined macrocyclic structure and highly crystalline. The directly obtained Na-MOSS powder crystals were proved to be submicrometer rod-like morphology. TGA results indicated that the initial decomposition temperature and residual weight at 800 °C of Na-MOSS were 427 °C and 89.6%, respectively. These results implied that Na-MOSS enjoyed superior thermal stability. Notably, we firstly discovered that the pyrolysis condensed products of Na-MOSS could react with $N_2$. Thereafter, the synthesized Na-MOSS was introduced into epoxy resin (EP) to improve the fire safety and decrease smoke hazards. Based on the cone calorimeter test results, with the incorporation of 2 wt% Na-MOSS, the peak of smoke production rate (p-SPR) and total smoke production (TSP) of EP/2 wt% Na-MOSS were apparently decreased by 50% and 36% compared with EP. Additionally, the storage modulus, flexural strength and modulus values of EP/Na-MOSS were higher than EP. The incorporation of Na-MOSS can apparently reduce the dielectric constant and loss of composites. These results indicate that EP/Na-MOSS enjoy better flame retardant, dielectric and mechanical properties and is more suitable for practical applications. Overall, our findings provide a class of overwhelmingly promising multifunctional rod-like macrocyclic organic–inorganic hybrid materials. Such materials can alleviate fire hazards and improve mechanical performance of EP composites.

## 1. Introduction

Epoxy resin (EP) as a crucial representative of thermosetting plastics, being extensively applied in industrial production, due to its superior chemical resistance, strong adherence and low manufacturing cost [1–3]. However, the flammability and heavy black smoke generated during combustion are the extremely critical problems faced by the industrial application of EP [4]. Therefore, considerable efforts have been devoted to develop efficient halogen-free flame retardants and smoke suppressants for EP [5–9]. Organic-inorganic hybrid silicon-containing compounds can be used as environmental-friendly flame retardants, due to their superior thermal stability and favorable compatibility with polymer substrate [10,11]. These compounds usually refer to polyhedral oligomeric silsesquioxane (POSS), incompletely condensed POSS ($T_7$-POSS), linear ladder-structured polysilsesquioxanes (L-PSQs) and cyclic ladder-like polyphenylsilsesquioxanes (cyc-PSQs), et. al.

The chemical structure of materials determines their macroscopic performances. Compared with linear compounds, although there is only one chemical bond difference in macrocyclic compounds [12]. Owing to the unique cyclic topology, macrocyclic compounds endow with some superior physical/chemical properties, such as small hydrodynamic volume [13], low viscosity [14] and high glass transition temperatures [15], which make they have promising application in the fields of supramolecular self-assembly, drugs, vitro display and heat-resistant polymers [16–22]. Typically, The concept of cyclic polysilsesquioxanes was first proposed by Scott in 1946 [23] and

* Corresponding authors at: National Engineering Technology Research Center of Flame Retardant Material, School of Materials, Beijing Institute of Technology, 5 South Zhongguancun Street, Haidian District, Beijing 100081, PR China.
*E-mail addresses:* zwc18@bit.edu.cn (W. Zhang), yrj@bit.edu.cn (R. Yang).

https://doi.org/10.1016/j.cej.2021.130566
Received 28 January 2021; Received in revised form 22 April 2021; Accepted 24 May 2021
Available online 28 May 2021

macrocyclic oligomeric silsesquioxanes (MOSS) were an intriguing class of organic–inorganic hybrid nanomaterials with a three-dimensional inorganic rigid cyclic structure composed of Si-O-Si [24–26]. Additionally, MOSS as one member of polysilsesquioxanes family, and they were prepared via the hydrolysis and polycondensation of $RSiCl_3$ or $RSi(OR')_3$ [27]. Similar to polyhedral oligomeric silsesquioxanes (POSS), the R substituent groups of MOSS could be designed to be non-reactive and reactive as needed [26,28].

As a traditional porous material, zeolites plays an irreplaceable role in the fields of gas separation, energy storage and catalyst [29]. Notably, polysilsesquioxanes molecule is similar to the secondary building units of zeolites, and numerous reports have suggested that polysilsesquioxanes can be regard as a typical nanoscale building block to construct porous multifunctional organic–inorganic nanomaterials [30–33]. Wu et al. adopted benzene and octavinylsilsesquioxane (OVS) to fabricate a hybrid porous material with adjustable porosity via Friedel-Crafts reaction [34]. Chen et al. reported that porous POSS-based polymer composites were prepared via the thermal hydrosilylation and polymerization of hydrogen-terminated silicon nanocrystals (ncSi:H) and vinyl-POSS [35]. Han and co-workers synthesized two kinds of MOSS with highly reactive groups and porous polysilsesquioxanes networks [24].

Although the above-mentioned early attempts have explored excellent porous polysilsesquioxanes materials, the POSS/MOSS with highly reactive bonds must be synthesized in advance. Thus, this inevitably increased the cost and complexity of the fabrication of target materials. In particular, our group recent works reported that increasing the amount of $LiOH{\cdot}H_2O$/NaOH tended to obtain lithium- and sodium-containing hepta-phenyl polyhedral oligomeric silsesquioxane based on the hydrolysis condensation of phenyltriethoxysilane, and the target products showed pleasurable smoke toxicity suppression for EP [36,37]. Fe/Co– containing polyhedral oligomeric silsesquioxane complexes (Fe/Co@POSS-COOH) with mesoporous structures also were successfully synthesized to decrease the emission of smoke of EP composites during combustion [38].

In addition, in recent years, with increasing attention to environmental protection issues, many halogen-free flame retardants were used to flame retard polymers, such as carbon nanotubes [39], layered double hydroxides [40], phosphorous flame retardant [41], montmorillonite [42]. These reports also confirmed that special metal elements have obvious smoke suppression effects on EP. Nonetheless, there are few reports focusing on the synthesis and application of alkali-metal-containing cyclic polysilsesquioxanes. Therefore, these compounds are required to be tremendously unexplored.

Inspired by these desires, in the present research, we first synthesized a series of methyl macrocyclic oligomeric silsesquioxane sodium salt (Na-MOSS) through the hydrolysis condensation of methyltrimethoxysilane (as illustrated in Scheme 1). The natural morphology and porosity of Na-MOSS powder was directly observed by scanning electron microscopy (SEM) and Brunauer-Emmett-Teller (BET). Meanwhile, Na-MOSS demonstrated excellent thermal stability. Na-MOSS was used as additives for EP, not only did enhance the mechanical properties of the resulted composites, but also effectively reduced the diffusion of heat, smoke and poisonous gas during combustion. Then, the detailed flame retardant and smoke suppression mechanism related to Na-MOSS were discussed as well. Indeed, the successfully synthesized Na-MOSS will open exciting opportunities for preparing smoke suppressant of high-performance EP composites.

## 2. Experimental section

### 2.1. Materials

Methyltrimethoxysilane (MTMS) (>97%) was purchased from Aladdin (China). Ethanol, $H_2O$ and NaOH were supplied by Beijing Chemical Works. Diglycidyl ether of bisphenol A (DGEBA, E44) (the chemical structure was shown in Scheme 2**b**) was supplied by FeiCheng DeYuan Chemicals Co., Ltd. 4,4-diaminodiphenylsulphone (DDS, >98.0%) (the chemical structure was displayed in Scheme 2**b**) was purchased from Tianjin Guangfu Fine Chemical Research Institute. All solvents and reagents were used as obtained without any further purification.

### 2.2. Molecular design and synthesis of Na-MOSS

100 mL of ethanol, 6.8 g of MTMS and 2.0 g of NaOH were stepwise added in a dry 250 mL three-necked flask. The resulting mixture was heated to 65 °C under agitating and was stirring for 18 h, then 1.8 mL of

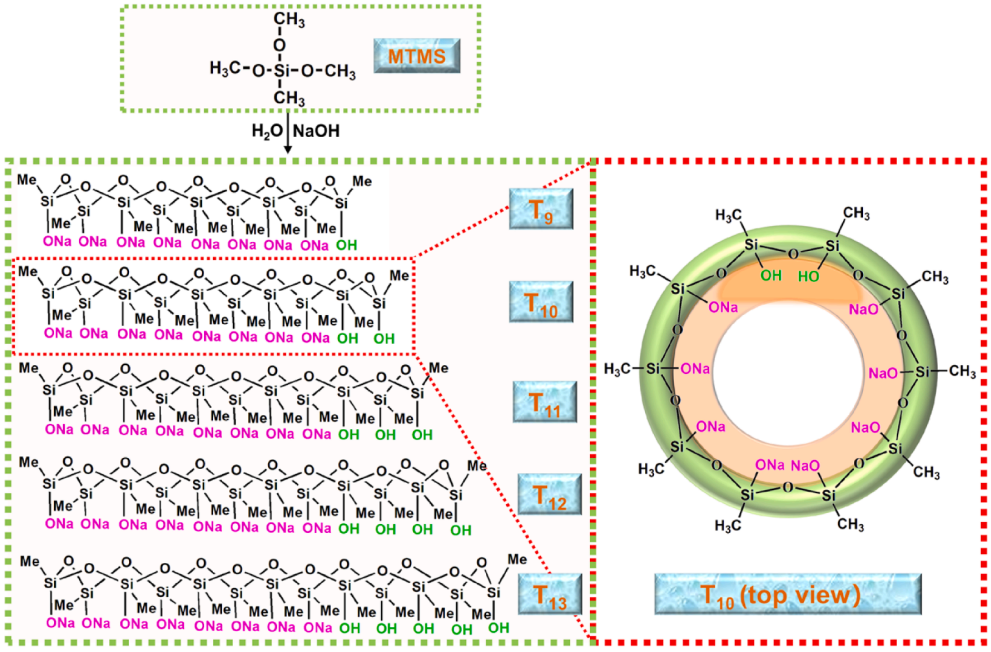


**Scheme 1.** The synthetic strategy and chemical formulas of a series of Na-MOSS (Me = $CH_3$).

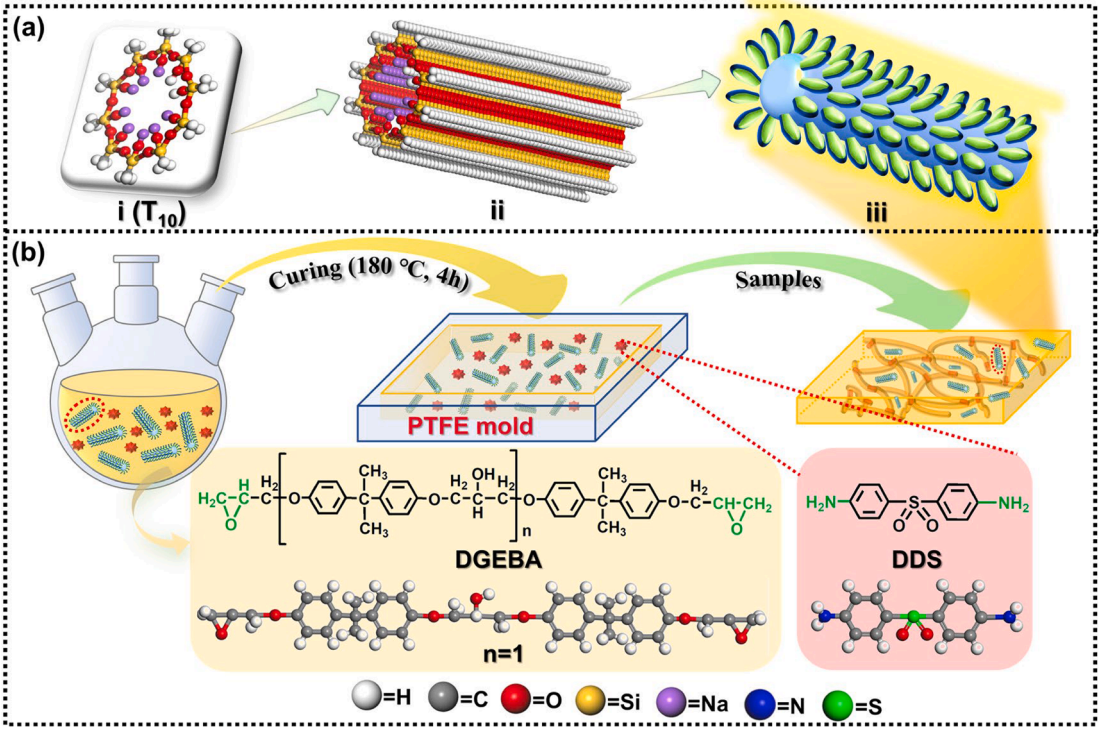


**Scheme 2.** Na-MOSS chemical structure model (a i), schematic diagram of atomic stacking (a ii) and natural morphology (a iii) of submicron rod-like structure Na-MOSS; the curing process of EP and EP/Na-MOSS (b).

distilled water was introduced and the solution was stirring for 4 h (white precipitate appeared about an hour later). Finally, the liquid was filtered off and the precipitate was washed with ethanol several times, then dried in a blast oven at 80 °C for 24 h to give a white solid powder. The synthetic route is shown in Scheme 1 and the characterization data of corresponding relative molecular mass is listed in Table S1.

### 2.3. Preparation of EP and EP/Na-MOSS

DGEBA (E-44) and Na-MOSS (chemical structure model is listed in Scheme 2**a**) powder were blended in a dry three-necked flask at 140 °C for 2 h. Thereafter, DDS as curing agent was added into the mixture and stirring for 40 min to dissolve it sufficiently. Finally, the samples were

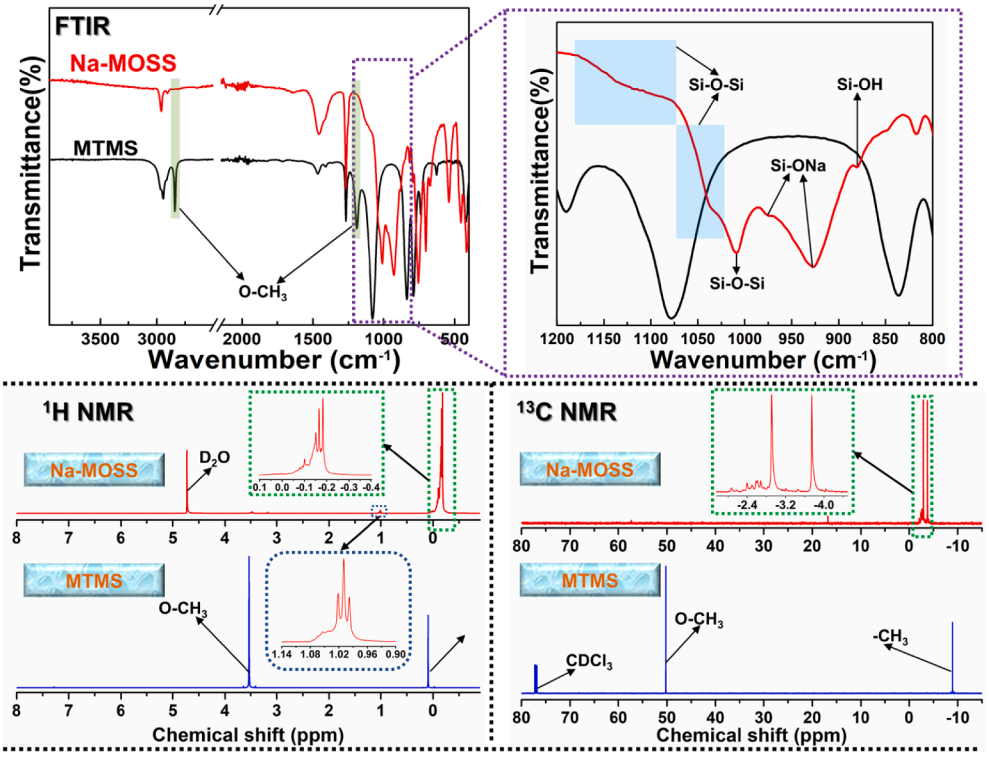


**Fig. 1.** FTIR, $^{1}$H and $^{13}$C NMR spectra of MTMS and Na-MOSS.

obtained through curing the mixture at 180 °C for 4 h. EP was prepared without incorporating Na-MOSS. Additionally, the curing process of EP/Na-MOSS is displayed in Scheme 2**b**, and the corresponding components are listed in Table S2.

### 2.4. Characterizations

The characterizations utilized in this work are displayed in the **Supplementary Information**.

## 3. Results and discussion

### 3.1. Molecular structure characterization of Na-MOSS

The FTIR, $^{1}H$ and $^{13}C$ NMR spectra of MTMS and Na-MOSS are displayed in Fig. 1. The characteristic peaks of O-$CH_3$ (MTMS) appear at 1190 and 2840 $cm^{-1}$, which are clearly disappeared in the FTIR spectra of Na-Me-POSS. Similarly, the resonance signal peaks at 3.53 and 50.34 ppm assign to the H and C atoms in O-$CH_3$, which are totally disappeared in the $^{1}H$ and $^{13}C$ NMR spectra of Na-MOSS. These results indicate that the hydrolysis reaction of MTMS is complete. Additionally, compared to the single sharp peak at 1078 $cm^{-1}$ (Si-O in MTMS), owing to the complex and various chemical conditions of the Si-O-Si bonds, the diverse broadened/sharp adsorption peaks appear at 1175–1000 $cm^{-1}$ in Na-MOSS [37,43–45]. In particular, a sharp peak at 928 $cm^{-1}$ belong to the stretching vibration of Si-O-Na, and a small characteristic peak at 880 $cm^{-1}$ correspond to the Si-OH structure [44,46,47]. Meanwhile, the multiple resonance signals of –$CH_3$ can been observed in the $^{1}H$ and $^{13}C$ NMR spectra of Na-MOSS, suggesting that the chemical environments of –$CH_3$ in Na-MOSS aren't identical. Furthermore, multiple signals at $\delta =$ 1.08–0.96 ppm are assigned to Si-OH [48]. Therefore, it is evident that Na is successfully grafted onto the Si-O bonds based on the chemical reaction among NaOH, $H_2O$ and MTMS.

Subsequently, as can been observed in Fig. 2**a, 29Si** NMR and MALDI-TOF-MS are adopted to further determine the chemical structure of Na-MOSS. In comparation with the $^{29}Si$ NMR spectra of MTMS, the signals of Si atoms of Na-MOSS present distinct changes. Specially, the peak at −41.06 ppm is assigned to the signals of Si atoms in the $CH_3$-Si-ONa fragments. Other three peaks are located at −49.06, −49.58 and −50.85 ppm, which attributed to the resonances of Si atoms in the $CH_3$-Si-OH fragments [48–50].

In addition, the convincing evidence of the structural information of macrocyclic Na-MOSS can be further provided by MALDI-TOF-MS. As illustrated in Fig. 2**b**, it is obvious that the difference of the two main molecular ion peaks is about 76, attributing to the repeated structural unit "$MeSiHO_2$". Additionally, it was reported that the hollow cavity of cyclic compounds could retain small molecules [51], and the solvent was used in MALDI-TOF-MS test was $H_2O$ endowed with the relative molecular mass of 18. The value is consistent with the difference of two adjacent peaks (such as 934.9 and 952.9). As listed in Table S1, every molecular ion peak is well assigned through calculation. Typically, taking $T_{10}$ as an example, as illustrated in the upper right corner of Fig. 2**b**, every peak has three main split peaks. The difference between the previous and next peak is about 1. Therefore, the average relative molecular mass (experimental value) of $T_{10}$ and $T_{10} + H_2O$ are 935.9 and 953.9, which extremely close to the theoretical calculated value of 936 ($T_{10}$) and 954 ($T_{10} + H_2O$). Meanwhile, Fig. 2**c** displays the ball and stick model of $T_{10}$ and $T_{10} + H_2O$ molecule of the macrocyclic Na-MOSS. Based on the above-mentioned comprehensive analysis, it is confirmed that a series of macrocyclic Na-MOSS are successfully synthesized.

### 3.2. Morphology and porosity analysis

The obtained Na-MOSS powder was directly coated on the conductive paste, the micromorphology and elemental composition of Na-MOSS were characterized by SEM and EDS. Submicrometer-sized rod-structured (with the diameter of ~270 nm) morphologies are observed by low-magnification SEM images (scale bars are 5 and 2 μm). High-magnification SEM images (Fig. 3**c and d**) suggest that the submicrometer-sized rod-like architectures are rely on the ordered self-

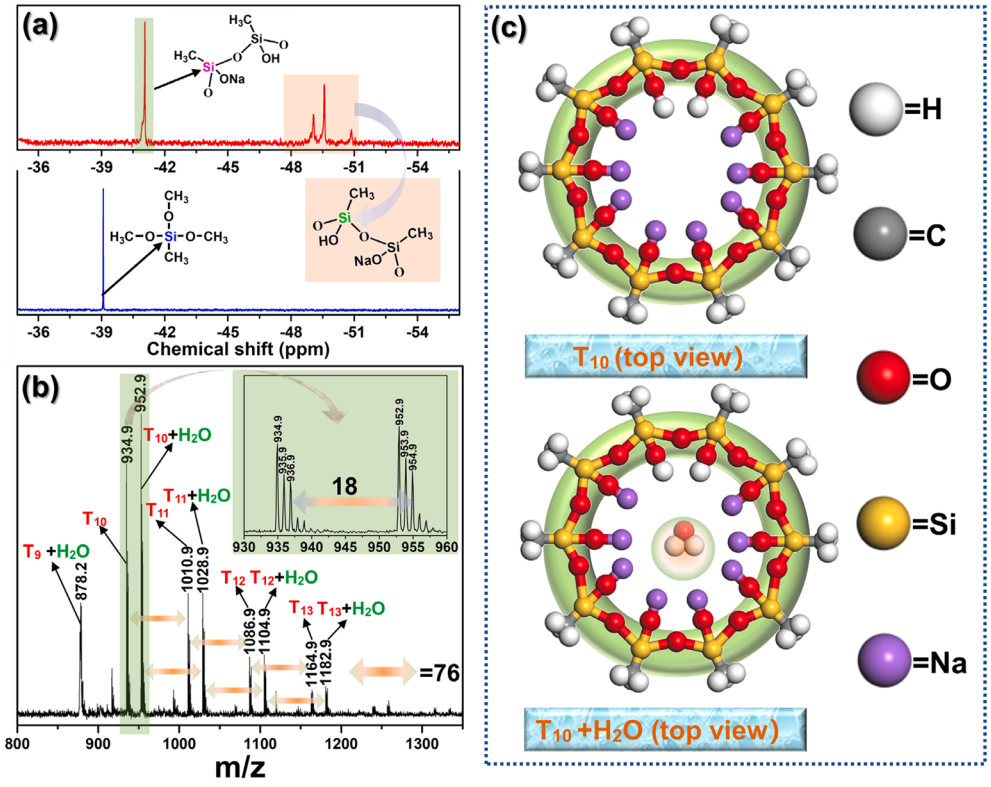


**Fig. 2.** $^{29}Si$ NMR (a) and MALDI-TOF-MS (b) spectra of Na-MOSS; the ball and stick model (c) of $T_{10}$ and $T_{10} + H_2O$ molecule.

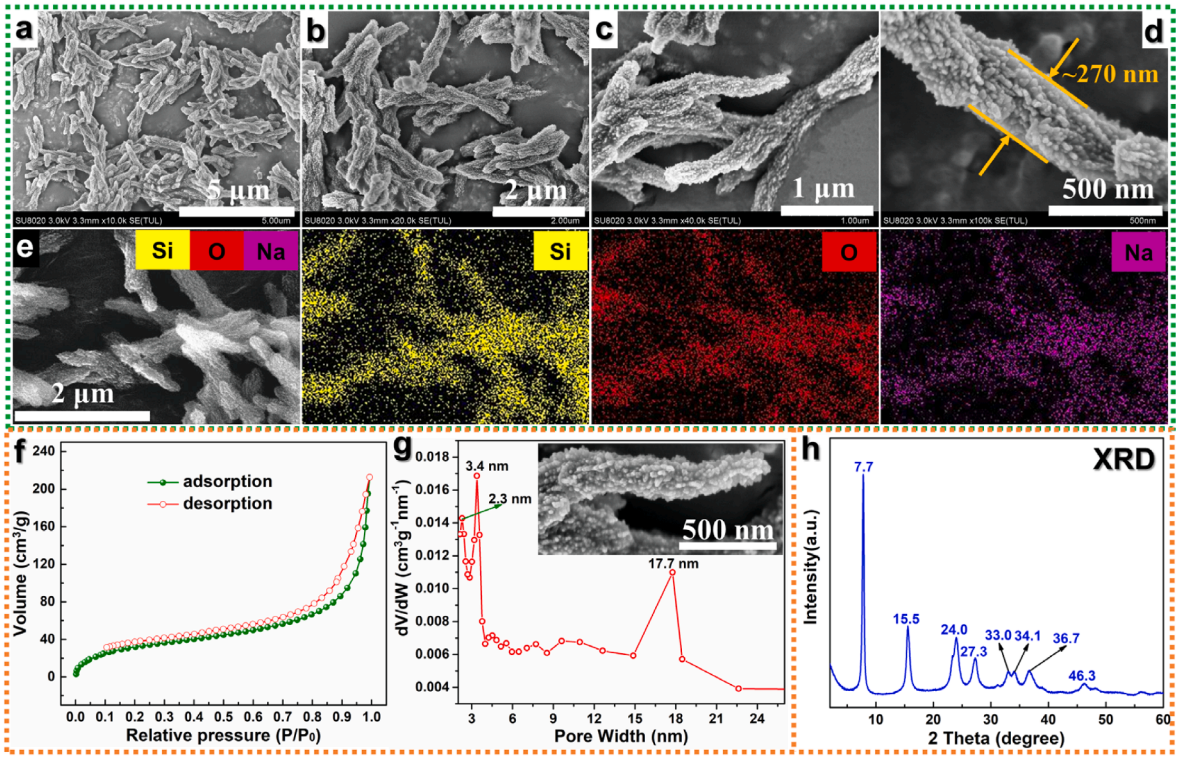


**Fig. 3.** SEM (a, b, c and d) and elemental mapping (e) images; nitrogen adsorption–desorption isotherms (f), pore size distributions (g) and XRD pattern (h) of Na-MOSS powder.

assembly of Na-MOSS nanorods with the size of about 20 nm. Furthermore, the uniform element distribution of Si, O and Na further verifies the submicrometer-sized rod-like assemblies is formed by Na-MOSS. Particularly, as illustrated Fig. 3**d** and **g** (inset), it is noteworthy that there are many slit-shaped pores distributing around the tightly packed Na-MOSS nanorods. The surface area and pore size distribution of Na-MOSS powder were studied by Brunauer-Emmett-Teller (BET) analytical method [52,53]. The specific surface area based on the BET multi-point method is up to 118.6 $m^2/g$. Fig. 3**f** displays the characteristic type IV isotherms curve, which endows with a precisely H3-type hysteresis loop appeared at high relative pressures ($P/P_0 > 0.8$). This typical feature reveals that Na-MOSS is a kind of mesoporous materials. Typically, the H3-type hysteresis loop suggests the appearance of large slit-shaped pores [54]. Furthermore, the calculated pore size distribution is based on the desorption branch of the Barrett-Joyner-Halenda (BJH) analysis [55]. As illustrated in Fig. 3**g**, only mesopore structures with the pore size of 2.3, 3.4, and 17.7 nm appeared in the formed Na-MOSS powder. The pore size of 17.7 nm is well consistent with the size of slit-shaped pores in SEM images (Fig. 3**d** and **g** (inset)). Additionally, the 2.3 and 3.4 nm of mesopores may closely associated with the

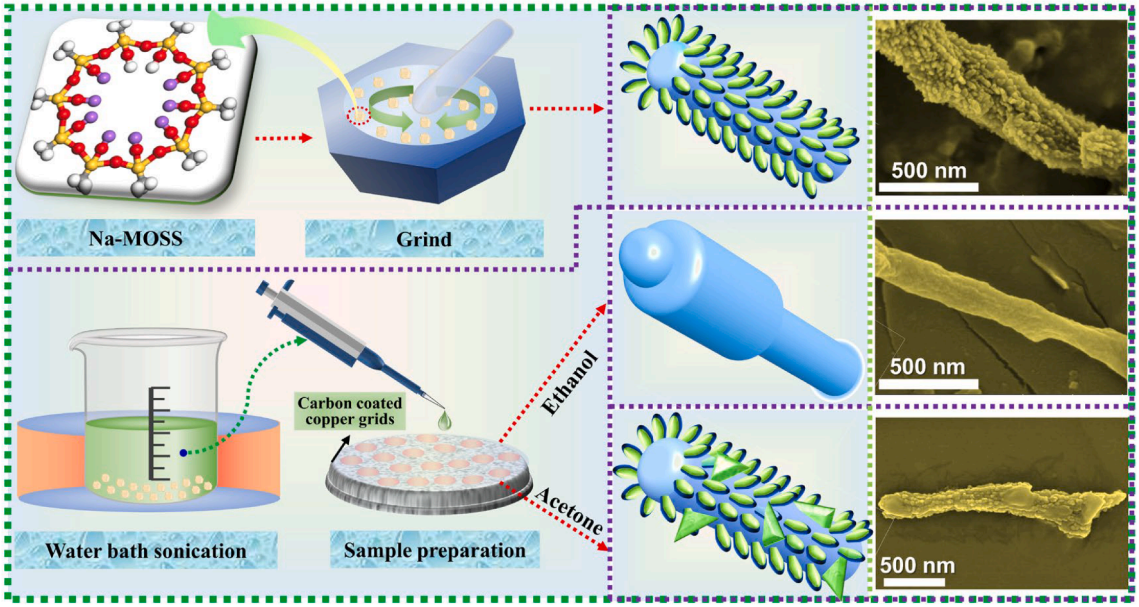


**Fig. 4.** The sample preparation and schematic diagram to present the morphology of Na-MOSS under different conditions.

polysilsesquioxanes natural structure [56,57]. Significantly, as displayed in X-ray diffraction (XRD) pattern (Fig. 3**h**), multiple sharp and strong diffraction peaks appear at 7.7, 15.5, 24.0, and 27.3°, which are assigned to the *d*-spacing values of 11.5, 5.7, 3.7, 3.3 Å, respectively. Meanwhile, these intense diffraction peaks indicate that the obtained Na-MOSS powder is highly crystalline.

In general, since the powder crystals of low-dimensional nanomaterials are exceedingly easy to agglomerate together, their true morphologies are bound to be affected and cannot be clearly observed. Therefore, the morphologies of low-dimensional nanomaterials are usually studied by the liquid exfoliation of powder crystals [58,59]. We also investigated the morphology of Na-MOSS in two different solvents. The specific sample preparation was as follows (Fig. 4): the Na-MOSS powder (0.5 mg) was incorporated into ethanol/acetone (15 mL), and the solution was placed in 50 °C water bath and sonication for 15 min. A small droplet of ethanol/acetone solution of Na-MOSS was dropped onto the carbon coated copper grids. The samples were supplied by evaporating their ethanol/acetone solution.

Specially, as can been observed in Fig. 5**a, b and c, a** large number of submicrometer-sized rods cover the entire field of vision, however, their diameters (at 110–200 nm) are apparently smaller than the rods formed by directly coating the Na-MOSS powder on the conductive adhesive. Notably, the surface of the rods is not smooth. Furthermore, the corresponding elemental maps give further proof that the generated submicrometer rods are Na-MOSS. The self-assembled morphologies of Na-MOSS in acetone solution assisted by sonication are observed in Fig. 5**g**, **h** and **i**, suggesting that the rough submicrometer rods with diameters of 150–250 nm. Meanwhile, the submicrometer rods are comprised of numerous nanoflakes and nanoroads. Compared with the morphology in ethanol dispersion, it is clearly that this morphology is closer to its original. In short, the types of solvent have an apparent effect on the formed morphological features of the resulting crystals.

### 3.3. Thermal properties of Na-MOSS

TG-FTIR technique was adopted to further analyze the thermal properties of Na-MOSS. As we all known, substances will be degraded during heating and accompanied by weight loss [60]. Surprisingly, as presented in Fig. 6**a**, the weight of Na-MOSS gradually increases with rising temperature (from ~ 550 °C) is first found in this system. Similarly, ranging in the temperature from 550 to 800 °C under air atmosphere (Fig. 6**c**), although the weight is slightly increased, it is not obvious. Therefore, the reasonable deduction for this phenomenon is that the pyrolysis products of Na-MOSS will react with $N_2$ in a relatively high-concentration nitrogen atmosphere. Additionally, the initial decomposition temperature (defined as the weight loss is 5%) and the residual weight at 800 °C of Na-MOSS ($N_2$ atmosphere) are 427 °C and 89.6% (Table S3), respectively. Therefore, Na-MOSS has an outstanding prospect for application in the field of flame retardant. Additionally, the degradation process of Na-MOSS is extremely sluggish in the range of 100–450 °C, so that there are hardly any visible infrared peaks of pyrolysis gases appearing in the three-dimensional (3D) TG-FTIR spectra. The most weight loss rate is occurred during the temperature range of 450–550 °C. Combining 3D TG-FTIR spectra (Fig. 6**b and d**) with FTIR

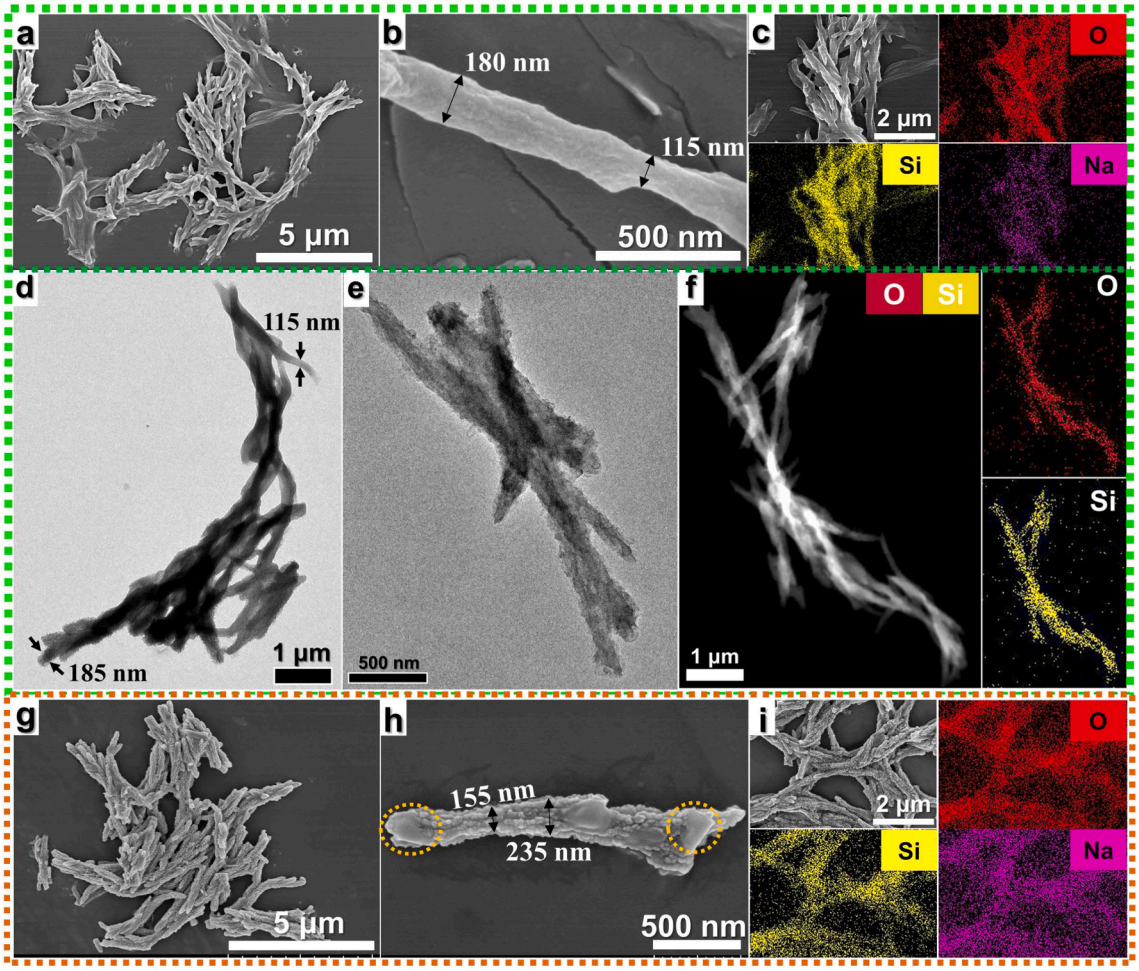


**Fig. 5.** SEM (a, b, c, g, h and i), TEM (d, e and f) images and the corresponding elemental maps of Na-MOSS in ethanol (a, b, c, d, e and f)/acetone (g, h and i) solution assisted by sonication.

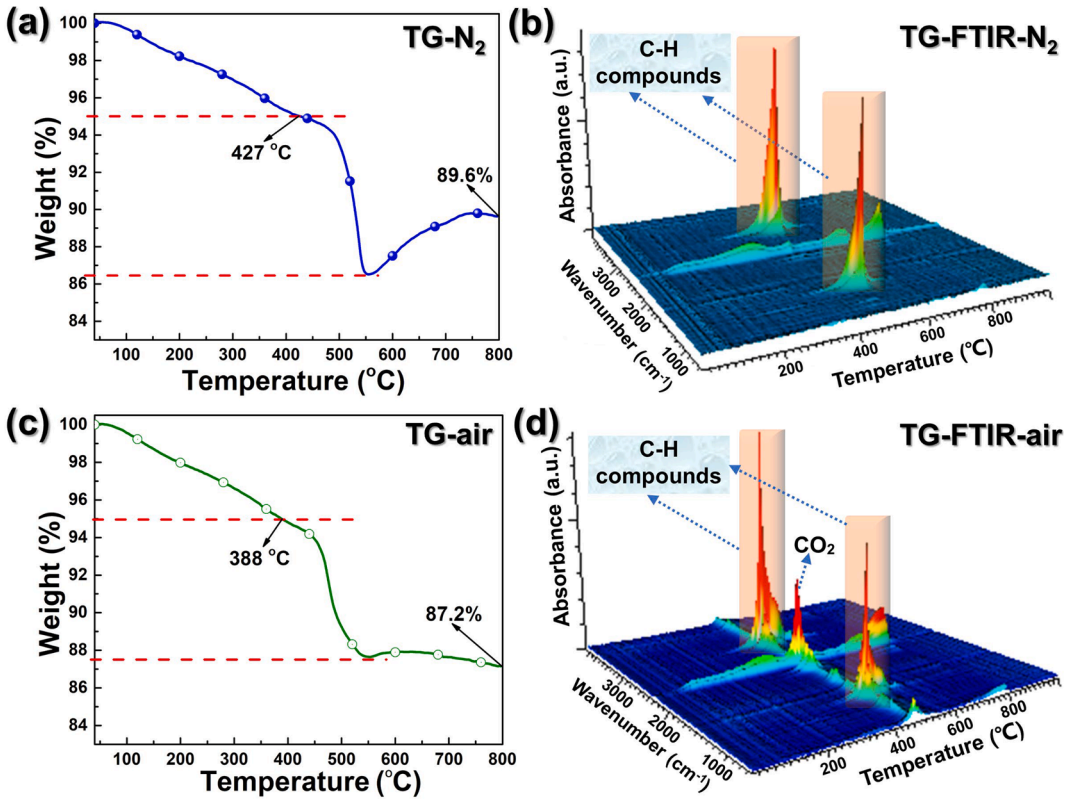


**Fig. 6.** TGA curves (a, c) and 3D TG-FTIR spectra (b, d) of Na-MOSS under $N_2$/air atmosphere.

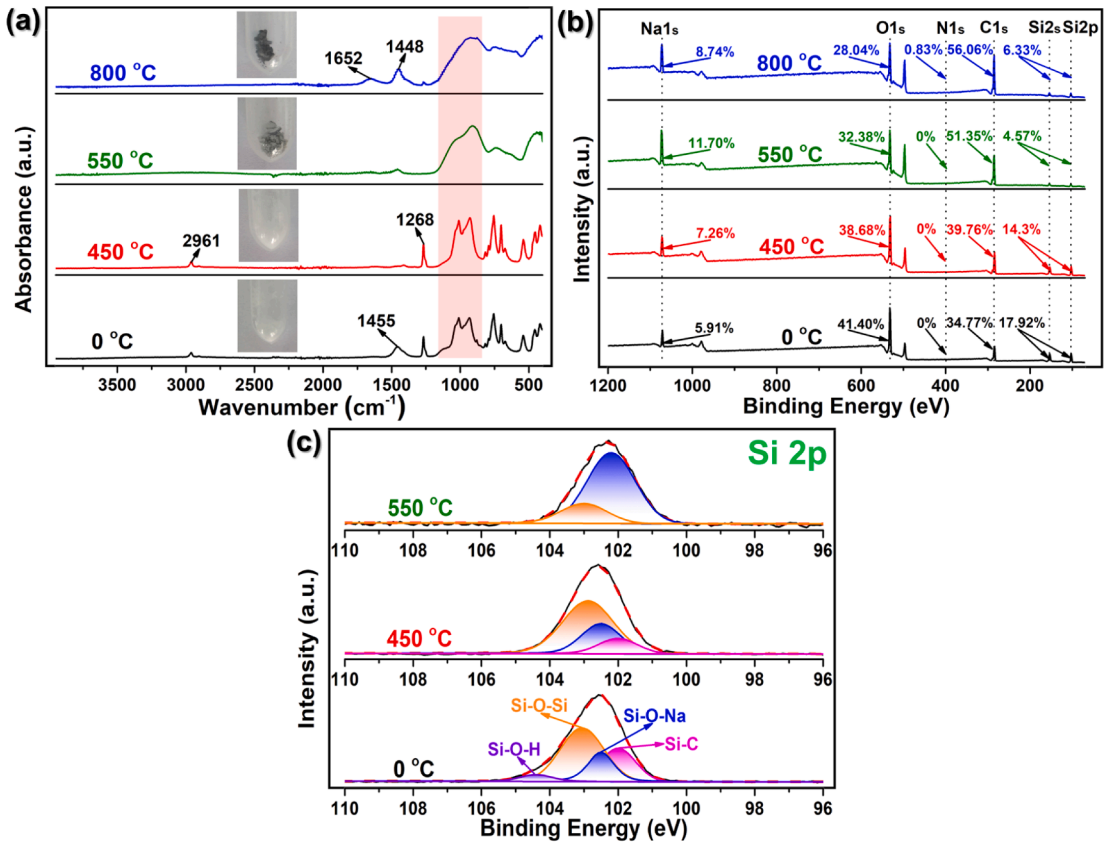


**Fig. 7.** The digital photos (a(inset)), dynamic FTIR, wide-scan and high-resolution Si 2p XPS spectra of condensed phase products.

spectra (Fig. S1) of pyrolytic volatile components at the maximum weight loss rate, the generated gaseous products are hydrocarbons (compounds containing C–H bonds) [61,62]. Additionally, the evolved volatiles of Na-MOSS under air atmosphere involve some other gas products, such a CO and $CO_2$.

In order to find the reason for the increase in weight within the temperature range of 550–800 °C, Fig. 7 display the FTIR, wide-scan and Si 2p high-resolution XPS spectra of the condensed phase products generated during the thermal degradation of Na-MOSS. Compared to the FTIR and Si 2p spectra of Na-MOSS at 0 °C, the peak at 880 $cm^{-1}$ (Fig. 7**a**) or 104.4 eV (Fig. 7**c**) is assigned to Si-OH which disappeared completely at 450 °C. Meanwhile, the characteristic absorption peak of C–H located at 1455 $cm^{-1}$ also disappeared totally.

Based on the above results, it can be inferred that this stage is ascribed to the elimination of $H_2O$ after the cross-linking of the Si-OH bonds in Na-MOSS molecule. It may also be the pyrolysis of some alkyl groups in the Na-MOSS molecule [63]. When the temperature rises to 550 °C, the peaks located at 2961 ($–CH_3$) and 1268 $cm^{-1}$ (C-Si) are disappeared completely. Meanwhile, the characteristic peak of Si-O-Si (1175–1000 $cm^{-1}$) broadens and shifts to lower wavenumbers. Similar results are observed in high-resolution Si2p XPS spectra. Additionally, the atomic concentration of Na and C significantly increase from 7.26%, 39.76% to 11.7%, 51.35%, respectively. While the atomic concentration of Si apparently decreases from 14.3% to 4.57%. Therefore, these results indicate that the thermal degradation process (450–550 °C) mainly involve the breakdown of the Si-O-Si cage, loss of $–CH_3$ groups, and cross-linking reactions. Specially, for the FTIR spectra of condensed phase products at 800 °C, a new peak appears at 1652 $cm^{-1}$, which belong to the stretching vibration of C-N bonds. Meanwhile, the wide-scan XPS spectra give further proof that nitrogen is doped in the char residue after calcination at 800 °C.

### 3.4. Fire safety of EP/Na-MOSS composites

As we all know, the main fire hazards are focused on the heat release, smoke production and poisonous volatiles emission. Cone calorimeter test was adopted to evaluate the flame retardant effect after incorporating Na-MOSS (1 and 2 wt%) into EP matrix. From the perspective of heat release and the emission of toxic gas CO, as displayed Fig. 8 and Table S4. Compared to EP, the peak of heat release rate (p-HRR) and peak of CO production rate (p-COP) of EP/2 wt% Na-MOSS are reduced by 14.3% and 25.0%, respectively. Meanwhile, Na-MOSS could make the value of p-HRR and p-COP of epoxy resin decrease slightly as gradually increasing the component of Na-MOSS. Notably, when the additional amount of Na-MOSS is only 1 wt%, the peak of smoke production rate (p-SPR) of EP/1 wt% Na-MOSS is apparently decreased to 0.27 $m^2/s$ compared with EP (p-SPR value is 0.44 $m^2/s$), and the reduction is 38.6%. Further increasing the addition amount to 2 wt%, the value of p-SPR for EP/2 wt% Na-MOSS dramatically reduce by 50%. the total smoke production (TSP) value of EP/2 wt% Na-MOSS also reduce by 36% compared with pure EP (TSP value is 36.8 $m^2$). In other words, Na-MOSS endows the formed EP composites with excellent smoke suppression effects at an exceedingly low addition. These results are highly consistent well with our previous work that sodium-containing POSS possess superior smoke retarding properties [36]. Additionally, as listed in Table S4, the LOI values of EP/1 wt% Na-MOSS and EP/2 wt% Na-MOSS are increased to 23.4% and 24.0%, slightly higher than that of pure EP (23.0%).

In general, the flame retardant and smoke suppression performance of polymer composites are closely related to the char residue generated during combustion. As shown in Fig. 8**e, f** and **g**, there is only a small amount of residual char remaining for EP after combustion, while the visible and apparent enhancement in the char residues of EP/1 wt% Na-MOSS and EP/2 wt% Na-MOSS. Additionally, EP produce a lot of black smoke during combustion can be attributed to its polyaromatic structure. The incorporation of Na-MOSS into EP promotes the cross-linked charring during combustion, so that more of these polyaromatic char residues are remained in the condensed phase. The formed compact char layers are not easy to be taken away by the generated volatiles, thus drastically reducing the smoke production. Therefore, the introduction of Na-MOSS into EP is exceedingly beneficial to reduce the diffusion of heat, CO and smoke during combustion, thereby mitigating the hazards

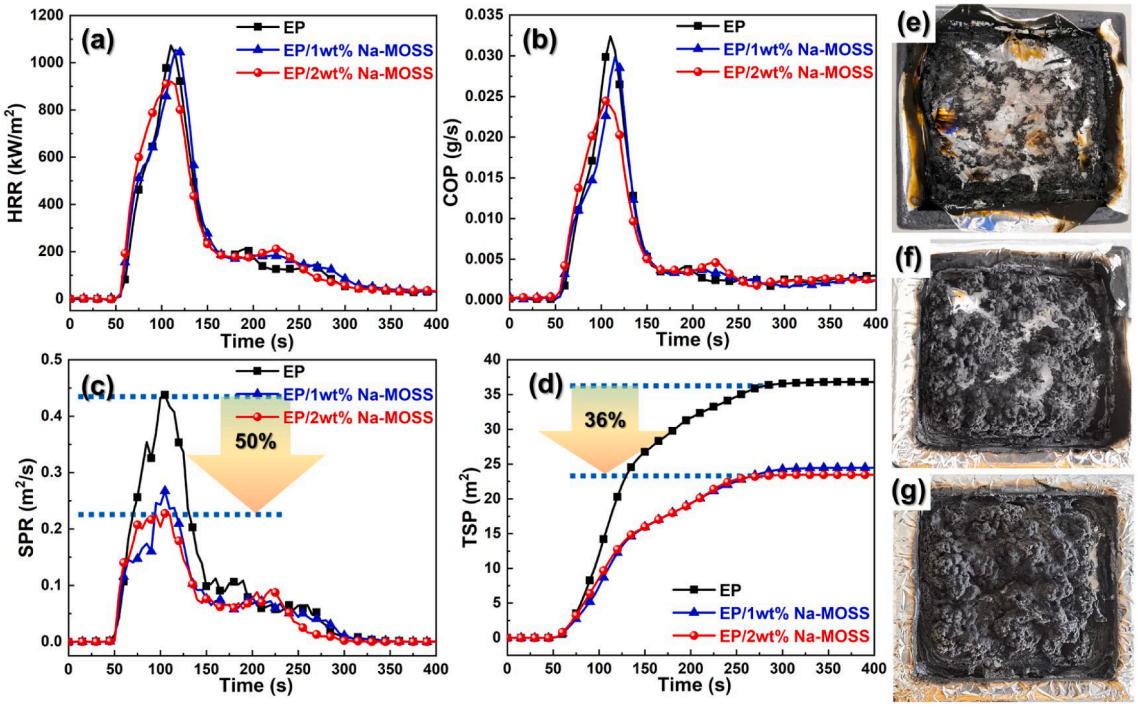


**Fig. 8.** HRR curves (a), COP curves (b), SPR curves (d) and TSP curves (d) of EP and EP/Na-MOSS composites; digital photos of char residues after cone calorimeter tests: EP (e), EP/1 wt% Na-MOSS (f) and EP/2 wt% Na-MOSS (g).

of fire accident.

### 3.5. Condensed phase products analysis

In order to further discover the intrinsic reason for the remarkable enhancement of smoke suppression performance of EP/2 wt% Na-MOSS. XRD, FTIR, Raman and XPS were utilized to characterize the chemical structure of char residues collected from cone calorimeter tests. Two wide diffraction peaks located at 23° and 43° both appear in the XRD patterns (Fig. 9**a**) of char residues of EP and EP/2 wt% Na-MOSS, which are assigned to the characteristic peaks of graphite carbon [64]. Moreover, EP and EP/2 wt% Na-MOSS present an obvious difference. Some additional sharp and intensive diffraction peaks are detected only for EP/2 wt% Na-MOSS and the positions of these diffraction peaks are different from Na-MOSS powder. Therefore, it can be inferred that Na-MOSS can acted as catalyst to promote the formation of highly crystalline and orderly char residue during combustion of EP matrix. Roman spectra (Fig. 9**b**) were further adopted to investigate the graphitization degree of the char residues of EP and EP/2 wt% Na-MOSS. Two typical peaks located at 1350 and 1596 $cm^{-1}$ are ascribed to the D-band and G-band, respectively. The graphitization degree is calculated by the integrated area ratio of D-band and G-band, so-called $I_D/I_G$. Specially, a lower value of $I_D/I_G$ is equal to a higher graphitization degree. The $I_D/I_G$ value of EP/2 wt% Na-MOSS is 1.33, apparently lower than that of EP (1.62). This result indicates that the char residue of EP/2 wt% Na-MOSS possessed more graphite phase carbon than EP.

Two weak and broad absorption peaks at 1586 and 731 $cm^{-1}$ can been seen in the FTIR spectra of char residues of EP and EP/2 wt% Na-MOSS, which are assigned to the polyaromatic structure [65]. This gives further proof that the yield of graphite carbon after burning EP or EP/2 wt% Na-MOSS. Additionally, for the FTIR spectra of EP/2 wt% Na-MOSS, a wide and strong characteristic peak located at 860–1280 $cm^{-1}$ is correspond to the stretching vibration of Si-O-Na (928 $cm^{-1}$), Si-O (1078 $cm^{-1}$) and C-Si (1268 $cm^{-1}$) groups. Particularly, a small weak peak appeared at 1456 $cm^{-1}$ belong to the stretching vibration of $Na_2CO_3$. The high-resolution Si 2p, C 1 s and O 1 s XPS spectra of char residues of EP/2 wt% Na-MOSS are illustrated in Fig. 9**d, e and f**, which further confirm the formation of Si-O-Si, Si-O-Na, C-Si, $Na_2CO_3$ and polyaromatic structure after burning EP/2 wt% Na-MOSS.

### 3.6. Flame retardant and smoke suppression mechanism

Generally, when the polymer composites with POSS are ignited, the organic polymer matrix on the heat radiating surface will be rapidly burned out. Then a gray-white heat-insulating char layer rich in $SiO_2$ is quickly produced on the surface of the substrate. Meanwhile, the generated $SiO_2$ will also serve as tiny solid particles to further increase the diffusion of smoke. In contrast, based on the above-detailed analysis, it is obviously observed that a black dense and strong char layer can be quickly formed after burning EP/Na-MOSS. Fig. 10 exhibits the possible flame retardant and smoke suppression mechanism. In the initial stage of combustion, the pyrolysis products of EP matrix and submicrometer-sized rod-structured Na-MOSS react with each other. Particularly, Na-MOSS is extremely alkaline, and $CO_2$ will be generated after burning organic polymer chains, thus a small amount of $Na_2CO_3$ is produced. Moreover, due to the catalytic charring of $Na_2CO_3$, accelerating the cross-linked charring of aromatic structures. As a result, black highly graphitized and crystalline char layers endowed with Si-O-Si, Si-O-Na, C-Si and polyaromatic structures are generated. Such attractive highly ordered thermally stable compact char layers are contribute to restrain the diffusion of smoke. Meanwhile, the high-quality char layers effectively inhibit heat and mass transfer and reduce the emission of the toxic volatiles. Finally, the submicrometer-sized rod-structured Na-MOSS used as promising smoke suppressant for EP can obtain excellent catalytic carbonization properties and improve fire safety.

### 3.7. Mechanical performance

In general, the incorporation of fillers will have a significant impact on the mechanical properties of polymer composites. DMA was applied to characterize the dynamic mechanical performance of EP, EP/1 wt% Na-MOSS and EP/2 wt% Na-MOSS. As seen in Fig. 11**a**, the glass transition temperatures ($T_g$ = the peak temperature in tan δ curve) of EP/1 wt% Na-MOSS and EP/2 wt% Na-MOSS are dramatically increased from 183.8 °C of EP to 192.1 and 194.7 °C, respectively. Additionally, the storage modulus values of EP/1 wt% Na-MOSS and EP/2 wt% Na-MOSS

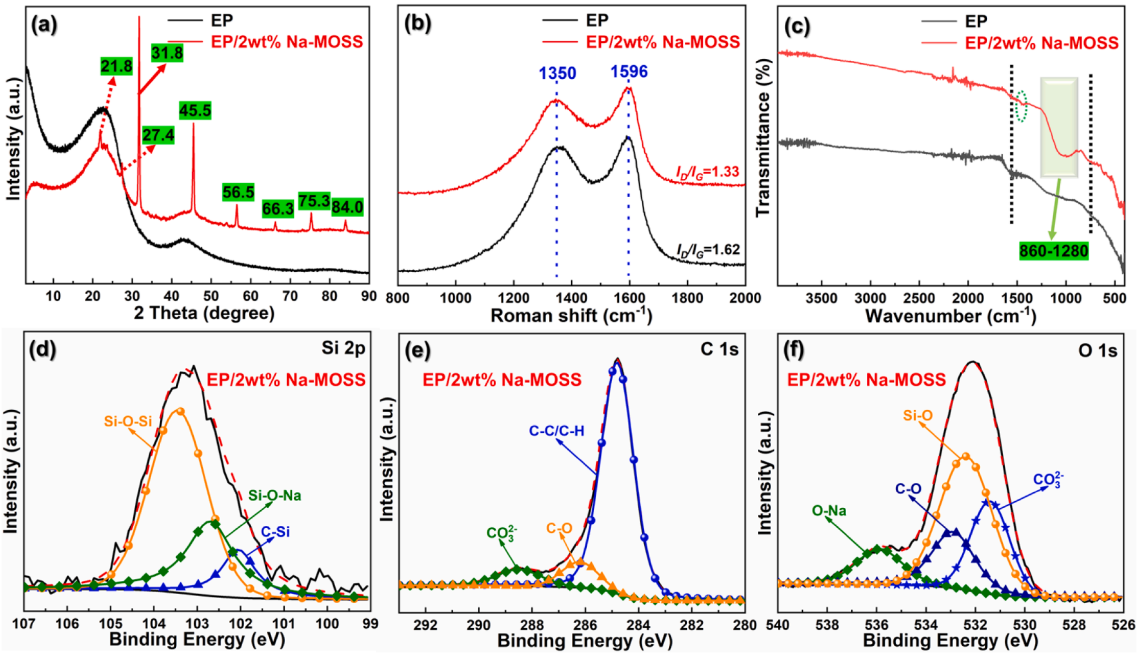


**Fig. 9.** XRD patterns (a), FTIR (b) and Raman (c) spectra of char residues of EP and EP/Na-MOSS; the high-resolution Si 2p (d), C 1 s (e) and O 1 s (f) XPS spectra of char residues of EP/2 wt% Na-MOSS.

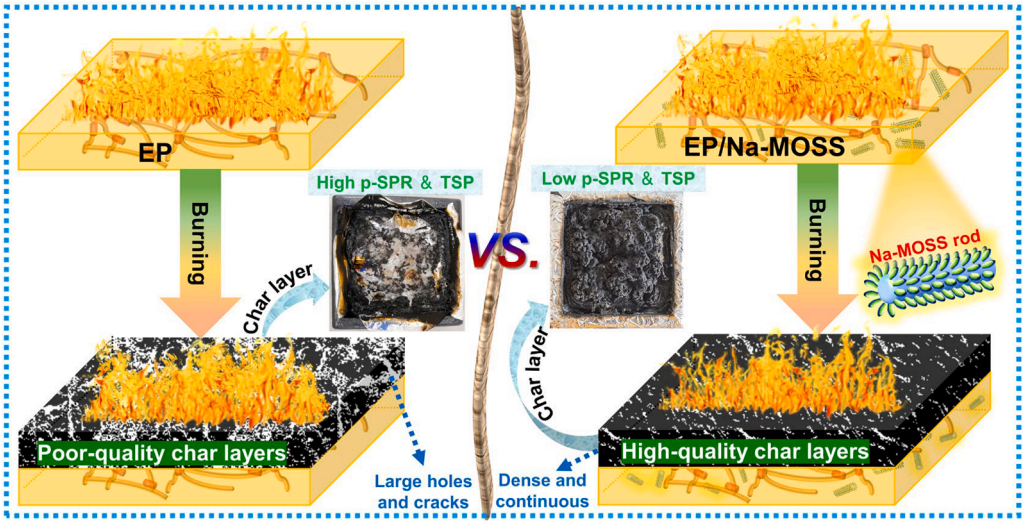


**Fig. 10.** Graphical illustration for the flame resistance and smoke suppression mechanism of EP/Na-MOSS.

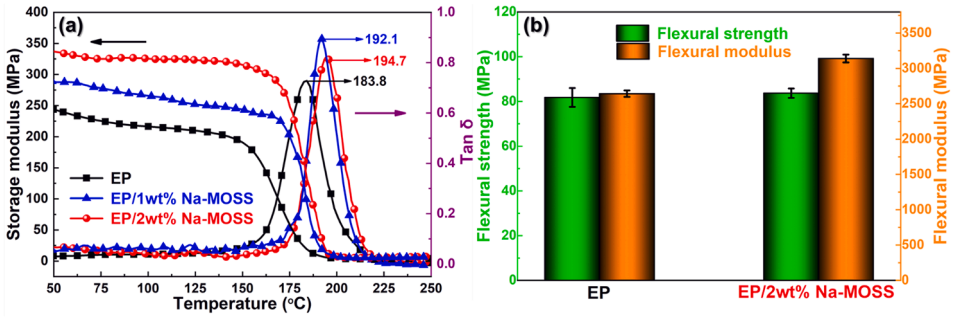


**Fig. 11.** DMA curves (a) of EP and EP/1 wt% Na-MOSS and EP/2 wt% Na-MOSS; flexural strength and modulus (b) of EP and EP/2 wt% Na-MOSS.

are also apparently improved compared to EP. Therefore, it is deduced that the delighted enhancements in the $T_g$ and storage modulus of EP/Na-MOSS are ascribed to the great stiffness of Na-MOSS and the improved interfacial interaction between the Na-MOSS submicrometer-sized rods and EP molecular chains. The flexural performance can be used as a crucial indicator to further determine the mechanical properties of EP/Na-MOSS composites. As displayed in Fig. 11**b**, the flexural strength of EP/2 wt% Na-MOSS is slightly increased from 81.8 MPa of EP to 83.7 MPa. Additionally, similar to the tendency of storage modulus, the flexural modulus of EP/2 wt% Na-MOSS is improved from 2643.9 MPa of EP to 3140.8 MPa. The enhancement of flexural strength and modulus of EP/2 wt% Na-MOSS may be ascribed to the excellent dispersion of Na-MOSS in EP. Therefore, the mechanical properties of EP/2 wt% Na-MOSS are not weakened or even enhanced after incorporating Na-MOSS.

### 3.8. Compatibility and dispersion

The Na-MOSS was added into epoxy resin at solid state, TEM was adopted to observe the microcosmic morphology of Na-MOSS and determine the dispersion state of Na-MOSS in EP matrix. As depicted in Fig. 12, Na-MOSS is still dispersed in the EP substrate in the form of submicrometer-sized rods, and there is no obvious large-scale agglomeration. However, few rods will be spliced together (a and b) and a slight agglomeration will be produced. Judging from the above-mentioned, this will not affect the enhancement of mechanical properties of EP/2 wt% Na-MOSS. Meanwhile, the diameter of the submicrometer-sized rods (c and c inset) dispersed in EP is well consistent with that in ethanol. In addition, the corresponding Si (e) and Na (f) elemental EDX line scan analyses of EP/2 wt% Na-MOSS certificate that the submicrometer-sized rod (d) is Na-MOSS.

### 3.9. Dielectric property

Since the synthesized Na-MOSS is a kind of salt, and Na-MOSS is easily soluble in $H_2O$, we further characterized the changes in the dielectric constant (ε′) and loss (tan δ) of EP composites after the incorporation of Na-MOSS. The dielectric constant curves (a) and dielectric loss curves (b) of EP and EP/Na-MOSS composites are displayed in Fig. 13. When Na-MOSS is introduced into EP, the dielectric constant values of EP/1 wt% Na-MOSS and EP/2 wt% Na-MOSS are both significantly reduced compared to pure EP, and the dielectric loss values are also decreased to a certain extent. Meanwhile, they show a trend of gradually decreasing as the additional content of Na-MOSS increases. The dielectric properties of polymer composites are closely related to the dispersibility, the polarity and reactivity of the filler. Therefore, the reasons for the reduction in dielectric constant and dielectric loss are as follows: Na-MOSS is well dispersed in the EP matrix and possesses a lot of weak polar structures such as Si-O-Si and $–CH_3$; the chemical reaction of the numerous Si-OH groups in Na-MOSS with the epoxy groups in DGEBA leads to a dramatically decrease in the interfacial polarization effect produced by epoxy functional groups [66,67].

## 4. Conclusions

In summary, the current report has fabricated a series of Na-MOSS through the hydrolysis condensation of MTMS in the presence of NaOH and $H_2O$. Thereafter, the synthesized Na-MOSS has been fully

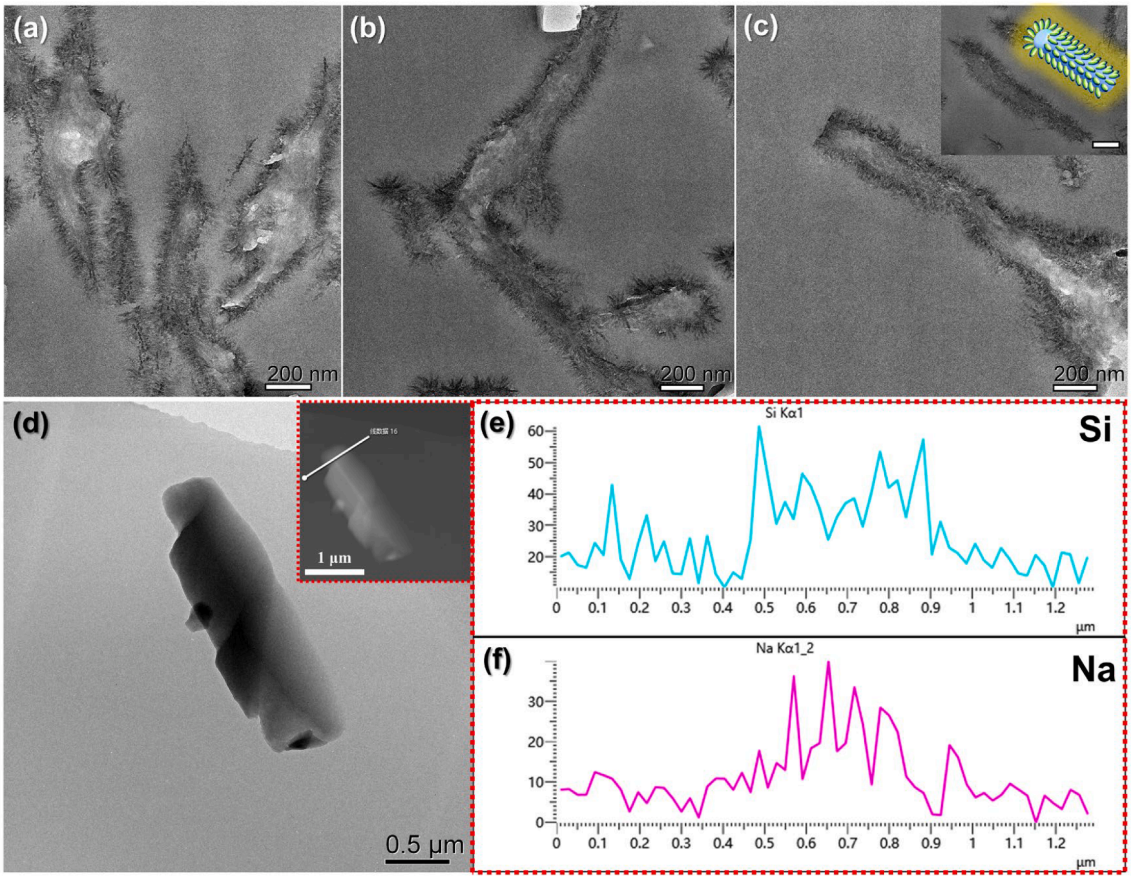


**Fig. 12.** TEM images (a, b, c and d) and the EDX line scan (e and f) analyses of EP/2 wt% Na-MOSS (scale bar is 200 nm (c inset)).

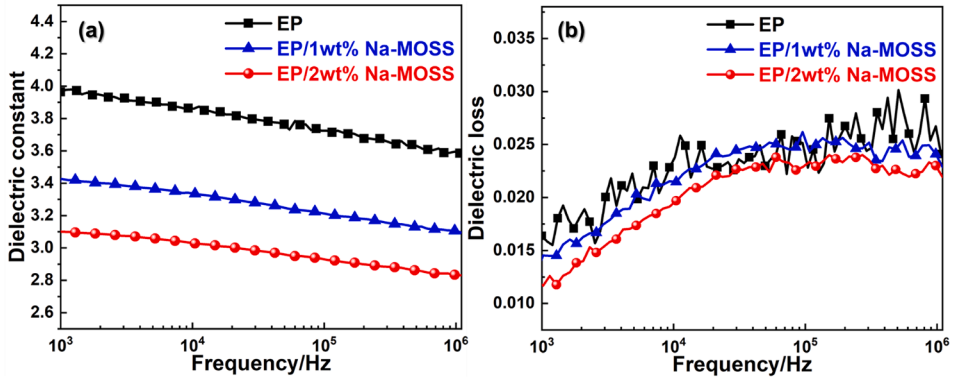


**Fig. 13.** The dielectric constant curves (a) and dielectric loss curves (b) of EP and EP/Na-MOSS composites.

proved to possess a precisely macrocyclic structure comprised of Si-O-Si. Specially, SEM and BET results show that Na-MOSS powder crystals present porous submicron rod-like morphology. Specially, this is the first research on the observation of crystalline morphology based on alkali-metal-containing macrocyclic oligomeric silsesquioxanes, and various solvents have an apparent effect on the formed rod- structured morphology of Na-MOSS. Surprisingly, contrary to the conventional theory, we firstly find that the residual weight of Na-MOSS gradually increases with the temperature (from ~ 550 °C) raises under nitrogen atmosphere. Similarly, the addition of Na-MOSS into EP could reduce the release of heat, toxic gases and smoke, especially for smoke production. Thereby, the fire hazards of the obtained EP/Na-MOSS composites are decreased. It is confirmed that the remarkable improvement of smoke suppression performance of EP/Na-MOSS closely related to the generation of highly graphitized and crystalline char layers endowed with Si-O-Si, Si-O-Na, C-Si and polyaromatic structures. Additionally, DMA, flexural strength, dielectric constant and loss tests proved that the mechanical and dielectric properties of EP/Na-MOSS had been significantly improved. The pleasurable enhancements in mechanical and dielectric properties are attributed to the high stiffness of Na-MOSS submicrometer-sized rods and the favorable interfacial interaction between the Na-MOSS and EP molecular chains. Therefore, the successful fabrication of submicrometer-sized rod-structured Na-MOSS not only expands the family of macrocyclic oligomeric silsesquioxanes, but also has a huge promotion significance for the preparation of EP composites endowed with superior comprehensive performances.

## Declaration of Competing Interest

The authors declare that they have no known competing financial interests or personal relationships that could have appeared to influence the work reported in this paper.

## Acknowledgments

This work was funded by the National Natural Science Foundation of China (No. 22075020 and No. 21975022).

## Appendix A. Supplementary data

Supplementary data to this article can be found online at https://doi.org/10.1016/j.cej.2021.130566.

## References

[1] P.Y. Kuo, M. Sain, N. Yan, Synthesis and characterization of an extractive-based bio-epoxy resin from beetle infested bark, Green. Chem. 16 (2014) 3483–3493.
[2] Y.J. Xu, L. Chen, W.H. Rao, M. Qi, D.M. Guo, W. Liao, Y.Z. Wang, Latent curing epoxy system with excellent thermal stability, flame retardance and dielectric property, Chem. Eng. J. 347 (2018) 223–232.
[3] X.H. Wu, S.L. Zheng, D.A. Bellido-Aguilar, V.V. Silberschmidt, Z. Chen, Transparent icephobic coatings using bio-based epoxy resin, Mater. Design. 140 (2018) 516–523.
[4] Y. Feng, C. He, Y. Wen, Y. Ye, X. Zhou, X. Xie, Y.W. Mai, Superior flame retardancy and smoke suppression of epoxy-based composites with phosphorus/nitrogen Co-doped graphene, J. Hazard. Mater. 346 (2018) 140–151.
[5] Y.S. Yuan, Y.T. Pan, Z.D. Zhang, W.C. Zhang, X.M. Li, R.J. Yang, Nickle nanocrystals decorated on graphitic nanotubes with broad channels for fire hazard reduction of epoxy resin, J. Hazard. Mater. 402 (2020), 123880.
[6] Z.D. Zhang, X.M. Li, Y.S. Yuan, Y.T. Pan, R.J. Yang, Confined dispersion of zinc hydroxystannate nanoparticles into layered bimetallic hydroxide nanocapsules and its application in flame-retardant epoxy nanocomposites, Acs Appl. Mater. Inter. 11 (2019) 40951–40960.
[7] Z.D. Zhang, J.Y. Qin, W.C. Zhang, Y.T. Pan, D.Y. Wang, R.J. Yang, Synthesis of a novel dual layered double hydroxide hybrid nanomaterial and its application in epoxy nanocomposites, Chem. Eng. J. 381 (2020), 122777.
[8] S.L. Qiu, B. Zou, T. Zhang, X. Ren, B. Yu, Y.F. Zhou, Y.C. Kan, Y. Hu, Integrated effect of $NH_2$-functionalized/triazine based covalent organic framework black phosphorus on reducing fire hazards of epoxy nanocomposites, Chem. Eng. J. 401 (2020), 126058.
[9] R.K. Jian, X.B. Lin, Z.Q. Liu, W. Zhang, J. Zhang, L. Zhang, Z. Li, D.Y. Wang, Rationally designed zinc borate@ZIF-8 core-shell nanorods for curing epoxy resins along with low flammability and high mechanical property, Compos. Part B-Eng. 200 (2020), 108349.
[10] W. Zhang, G. Camino, R. Yang, Polymer/polyhedral oligomeric silsesquioxane (POSS) nanocomposites: an overview of fire retardance, Prog. Polym. Sci. 67 (2017) 77–125.
[11] X. Wang, W. Zhang, Z. Qin, R. Yang, Optically transparent and flame-retarded polycarbonate nanocomposite based on diphenylphosphine oxide-containing polyhedral oligomeric silsesquioxanes, Compos. Part A-Appl. S. 117 (2019) 92–102.
[12] Z. Liu, Y. Huang, X. Zhang, X. Tu, M. Wang, L. Ma, B. Wang, J. He, P. Ni, H. Wei, Fabrication of cyclic brush copolymers with heterogeneous amphiphilic polymer brushes for controlled drug release, Macromolecules 51 (19) (2018) 7672–7679.
[13] J.M. Garcia Bernal, M.M. Tirado, J.J. Freire, J. Garcia de la Torre, Monte Carlo calculation of hydrodynamic properties of linear and cyclic polymers in good solvents, Macromolecules 24 (2) (1991) 593–598.
[14] Y.X. Chen, H. Miao, Completely recyclable biopolymers with linear and cyclic topologies via ring-opening polymerization of gamma-butyrolactone, Nat. Chem. 8 (2016) 42–129.
[15] Y.e. Cai, J. Lu, F. Zhou, X. Zhou, N. Zhou, Z. Zhang, X. Zhu, Cyclic amphiphilic random copolymers bearing azobenzene side chains: facile synthesis and topological effects on self-assembly and photoisomerization, Macromol. Rapid. Comm. 35 (9) (2014) 901–907.
[16] D. Prochowicz, A. Kornowicz, J. Lewiński, Correction to interactions of native cyclodextrins with metal ions and inorganic nanoparticles: fertile landscape for chemistry and materials science, Chem. Rev. 118 (2018) 13461–13501.
[17] S.S. Kale, M. Bergeron-Brlek, Y. Wu, M.G. Kumar, M.V. Pham, J. Bortoli, J. Vesin, X.-D. Kong, J.F. Machado, K. Deyle, P. Gonschorek, G. Turcatti, L. Cendron, A. Angelini, C. Heinis, Thiol-to-amine cyclization reaction enables screening of large libraries of macrocyclic compounds and the generation of sub-kilodalton ligands, Sci. Adv. 5 (8) (2019) eaaw2851, https://doi.org/10.1126/sciadv.aaw2851.
[18] K. Deyle, X.D. Kong, C. Heinis, Phage selection of cyclic peptides for application in research and drug development, Acc. Chem. Res. 50 (2017) 1866–1874.
[19] R.D. Taylor, M. Rey-Carrizo, T. Passioura, H. Suga, Identification of nonstandard macrocyclic peptide ligands through display screening, Drug. Discov. Today. 26 (2017) 17–23.
[20] H. Bai, J. Wang, Z. Li, G. Tang, Macrocyclic compounds for drug and gene delivery in immune-modulating therapy, Int. J. Mol. Sci. 20 (2019) 2097.
[21] W.C. Zhang, X.X. Wang, Y.W. Wu, Z. Qi, R.J. Yang, Preparation and characterization of organic-inorganic hybrid macrocyclic compounds: cyclic ladder-like polyphenylsilsesquioxanes, Inorg. Chem. 57 (2018) 3883–3892.
[22] N. Grassie, I.G. Macfarlane, The thermal degradation of polysiloxanes-I. Poly (dimethylsiloxane), Eur. Polym. J. 14 (1978) 875–884.
[23] W. Donald, Equilibria between linear and cyclic polymers in methylpolysiloxanes, J. Am. Chem. Soc. 68 (1946) 2294–2298.
[24] H. Jin, S. Zheng, Highly porous polysilsesquioxane networks via hydrosilylative polymerization of macrocyclic oligomeric silsesquioxanes, Macromolecules 41 (2008) 4561–4564.
[25] H. Jin, L. Zhu, S. Zheng, Synthesis and characterization of organic-inorganic macrocyclic molecular brushes with poly(ε-caprolactone) side chains, Eur. Polym. J. 48 (2012) 730–742.
[26] B.M. White, W.P. Watson, E.E. Barthelme, H.W. Beckham, Synthesis and efficient purification of cyclic poly(dimethylsiloxane), Macromolecules 35 (2002) 5345–5348.
[27] Y. Pozdniakova, K. Lyssenko, A. Korlyukov, I. Blagodatskikh, N. Auner, D. Katsoulis, O. Shchegolikhina, Alkali-metal-directed hydrolytic condensation of trifunctional phenylalkoxysilanes, Eur. J. Inorg. Chem. 2004 (6) (2004) 1253–1261.
[28] Y. Yi, N. Liu, L. Li, S. Zheng, A novel functionalized stereoregular macrocyclic oligomeric silsesquioxane: synthesis and its fast self-crosslinking via thiol-ene radical addition polymerization, Rsc Adv. 6 (2016) 87802–87807.
[29] Y. Zhang, S. Che, π–π Interactions between aromatic groups in amphiphilic molecules: directing hierarchical growth of porous zeolites, Angew. Chem. Int. Edit. 59 (1) (2020) 50–60.
[30] C. Zhang, F. Babonneau, C. Bonhomme, R.M. Laine, C.L. Soles, H.A. Hristov, A. F. Yee, Highly porous polyhedral silsesquioxane polymers. synthesis and characterization, J. Am. Chem. Soc. 120 (1998) 8380–8391.
[31] W. Chaikittisilp, M. Kubo, T. Moteki, A. Sugawara-Narutaki, A. Shimojima, T. Okubo, Porous siloxane-organic hybrid with ultrahigh surface area through simultaneous polymerization-destruction of functionalized cubic siloxane cages, J. Am. Chem. Soc. 133 (2011) 13832–13835.
[32] L. Zhang, H. Abbenhuis, Q. Yang, Y.M. Wang, P. Magusin, B. Mezari, R.A. van Santen, C. Li, Mesoporous organic-inorganic hybrid materials built using polyhedral oligomeric silsesquioxane blocks, Angew. Chem. Int. Edit. 46 (2007) 5003–5006.
[33] M. Seino, W. Wang, J.E. Lofgreen, D.P. Puzzo, T. Manabe, G.A. Ozin, Low-k periodic mesoporous organosilica with air walls: POSS-PMO, J. Am. Chem. Soc. 133 (45) (2011) 18082–18085.
[34] Y. Wu, D. Wang, L. Li, W. Yang, S. Feng, H. Liu, Hybrid porous polymers constructed from octavinylsilsesquioxane and benzene via Friedel-Crafts reaction: tunable porosity, gas sorption, and postfunctionalization, J. Mater. Chem. A. 2 (7) (2014) 2160–2167.
[35] D. Chen, W. Sun, C. Qian, L.M. Reyes, A.P.Y. Wong, Y. Dong, J. Jia, K.K. Chen, G. A. Ozin, Porous NIR photoluminescent silicon nanocrystals-POSS composites, Adv. Funct. Mater. 26 (2016) 5102–5110.
[36] X. Ye, J. Li, W. Zhang, R. Yang, J. Li, Fabrication of eco-friendly and multifunctional sodium-containing polyhedral oligomeric silsesquioxane and its flame retardancy on epoxy resin, Compos. Part B-Eng. 191 (2020) 107961, https://doi.org/10.1016/j.compositesb:2020.107961.
[37] X. Ye, W. Zhang, R. Yang, J. He, J. Li, F. Zhao, Facile synthesis of lithium containing polyhedral oligomeric phenyl silsesquioxane and its superior performance in transparency, smoke suppression and flame retardancy of epoxy resin, Compos. Sci. Technol. 189 (2020) 108004, https://doi.org/10.1016/j.compscitech.2020.108004.
[38] W. Zhang, W. Zhang, Y.-T. Pan, R. Yang, Facile synthesis of transition metal containing polyhedral oligomeric silsesquioxane complexes with mesoporous structures and their applications in reducing fire hazards, enhancing mechanical and dielectric properties of epoxy composites, J. Hazard. Mater. 401 (2021) 123439, https://doi.org/10.1016/j.jhazmat.2020.123439.
[39] J. Zhang, Q. Kong, D.-Y. Wang, Simultaneously improving the fire safety and mechanical properties of epoxy resin with Fe-CNTs via large-scale preparation, J. Mater. Chem. A. 6 (15) (2018) 6376–6386.
[40] J. Ding, Y.i. Zhang, X. Zhang, Q. Kong, J. Zhang, H. Liu, F. Zhang, Improving the flame-retardant efficiency of layered double hydroxide with disodium phenylphosphate for epoxy resin, J. Therm. Anal. Calorim. 140 (1) (2020) 149–156.
[41] Q. Kong, Y. Sun, C. Zhang, H. Guan, J. Zhang, D.Y. Wang, F. Zhang, Ultrathin iron phenyl phosphonate nanosheets with appropriate thermal stability for improving fire safety in epoxy, Compos. Sci. Technol. 182 (2019), 107748.
[42] Q. Kong, T. Wu, H. Zhang, Y. Zhang, M. Zhang, T. Si, L. Yang, J. Zhang, Improving flame retardancy of IFR/PP composites through the synergistic effect of organic montmorillonite intercalation cobalt hydroxides modified by acidified chitosan, Appl. Clay. Sci. 146 (2017) 230–237.
[43] Y. Wang, R. Qu, F. Pan, X. Jia, C. Sun, C. Ji, Y. Zhang, K. An, Y. Mu, Preparation and characterization of thiol- and amino-functionalized polysilsesquioxane coated poly(p-phenylenetherephthal amide) fibers and their adsorption properties towards Hg(II), Chem. Eng. J. 317 (2017) 187–203.
[44] N. Prigyai, S. Chanmungkalakul, V. Ervithayasuporn, N. Yodsin, S. Jungsuttiwong, N. Takeda, M. Unno, J. Boonmak, S. Kiatkamjornwong, Lithium-templated formation of polyhedral oligomeric silsesquioxanes (POSS), Inorg. Chem. 58 (2019) 15110–15117.

[45] K. Ohno, S. Sugiyama, K. Koh, Y. Tsujii, T. Fukuda, M. Yamahiro, H. Oikawa, Y. Yamamoto, N. Ootake, K. Watanabe, Living radical polymerization by polyhedral oligomeric silsesquioxane-holding initiators: precision synthesis of tadpole-shaped organic/inorganic hybrid polymers, Macromolecules 37 (2004) 8517–8522.
[46] M.T. Hay, B. Seurer, D. Holmes, A. Lee, A novel linear titanium(IV)-POSS coordination polymer, Macromolecules 43 (2010) 2108–2110.
[47] M.S. Dronova, A.N. Bilyachenko, A.I. Yalymov, Solvent-controlled synthesis of tetranuclear cage-like copper(II) silsesquioxanes. Remarkable features of the cage structures and their high catalytic activity in oxidation with peroxides, Dalton. T. 43 (2013).
[48] C. Krempner, H. Reinke, K. Weichert, Synthesis and structure of cyclic aluminum disiloxides, Organometallics 26 (2007) 1386–1392.
[49] H. Dong, M. Lee, R.D. Thomas, Z. Zhang, D.W. Mueller, Methyltrimethoxysilane sol-gel polymerization in acidic ethanol solutions studied by $^{29}$Si NMR spectroscopy, J. Sol-Gel Sci. Techn. 28 (2003) 5–14.
[50] N. Hurkes, C. Bruhn, F. Belaj, R. Pietschnig, Silanetriols as powerful starting materials for selective condensation to bulky POSS cages, Organometallics 33 (2014) 7299–7306.
[51] D. Ikuta, Y. Hirata, S. Wakamori, H. Shimada, Y. Tomabechi, Y. Kawasaki, K. Ikeuchi, T. Hagimori, S. Matsumoto, H. Yamada, Conformationally supple glucose monomers enable synthesis of the smallest cyclodextrins, Science 364 (6441) (2019) 674–677.
[52] Y.-T. Pan, L.u. Zhang, X. Zhao, D.-Y. Wang, Interfacial engineering of renewable metal organic framework derived honeycomb-like nanoporous aluminum hydroxide with tunable porosity, Chem. Sci. 8 (5) (2017) 3399–3409.
[53] P. Sangtrirutnugul, T. Chaiprasert, W. Hunsiri, T. Jitjaroendee, P. Songkhum, K. Laohhasurayotin, T. Osotchan, V. Ervithayasuporn, Tunable porosity of cross-linked-polyhedral oligomeric silsesquioxane supports for palladium-catalyzed aerobic alcohol oxidation in water, Acs Appl. Mater. Inter. 9 (14) (2017) 12812–12822.
[54] Z.Y. Xiong, C.L. Liao, X.G. Wang, Self-assembled macroporous coagulation graphene network with high specific capacitance for supercapacitor applications, J. Mater. Chem. A. 2 (2014) 19141–19144.
[55] A.-H. Lu, W. Schmidt, N. Matoussevitch, H. Bönnemann, B. Spliethoff, B. Tesche, E. Bill, W. Kiefer, F. Schüth, Nanoengineering of a magnetically separable hydrogenation catalyst, Cheminform 43 (33) (2004) 4303–4306.
[56] N. Zhang, X. Lei, T. Huang, L. Su, L. Zhang, Z. Xie, X. Wu, Guanidyl-functionalized polyhedral oligomeric silsesquioxane porous hybrid polymer coating for specific solid phase microextraction of phthalate esters in foodstuff, Chem. Eng. J. 386 (2020) 124003, https://doi.org/10.1016/j.cej.2019.124003.
[57] Y. Du, M. Unno, H. Liu, Hybrid nanoporous materials derived from ladder- and cage-type silsesquioxanes for water treatment, ACS Appl. Nano Mater. 3 (2) (2020) 1535–1541.
[58] X. Cai, Y. Luo, B. Liu, H.-M. Cheng, Preparation of 2D material dispersions and their applications, Chem. Soc. Rev. 47 (16) (2018) 6224–6266.
[59] J.N. Coleman, M. Lotya, A. O'Neill, S.D. Bergin, P.J. King, U. Khan, K. Young, A. Gaucher, S. De, R.J. Smith, I.V. Shvets, S.K. Arora, G. Stanton, H.-Y. Kim, K. Lee, G.T. Kim, G.S. Duesberg, T. Hallam, J.J. Boland, J.J. Wang, J.F. Donegan, J. C. Grunlan, G. Moriarty, A. Shmeliov, R.J. Nicholls, J.M. Perkins, E.M. Grieveson, K. Theuwissen, D.W. McComb, P.D. Nellist, V. Nicolosi, Two-dimensional nanosheets produced by liquid exfoliation of layered materials, Science 331 (6017) (2011) 568–571.
[60] P.K. Behera, P. Mondal, N.K. Singha, Self-healable and ultrahydrophobic polyurethane-POSS hybrids by diels-alder "Click" reaction: a new class of coating material, Macromolecules 51 (13) (2018) 4770–4781.
[61] P.A. Song, G.R. Chen, Y.M. Yu, Z.P. Fang, W.W. Lei, S.Y. Fu, H. Wang, Z.G. Chen, Bioinspired design of strong, tough, and thermally stable polymeric materials via nanoconfinement, ACS nano 12 (2018) 9266–9278.
[62] W.C. Zhang, G. Ferraro, R.J. Yang, FTIR and GCMS analysis of epoxy resin decomposition products feeding the flame during UL-94 standard flammability test. Application to the understanding of the blowing-out effect in epoxy/polyhedral silsesquioxane formulations, J. Anal. Appl. Pyrol. 135 (2018) 271–280.
[63] Y.J.X.Z.M. Zhu, W. Liao, S.M. Xu, Y.Z. Wang, Highly flame retardant expanded polystyrene foams from phosphorus-nitrogen-silicon synergistic adhesives, Ind. Eng. Chem. Res. 56 (2017) 4649–4658.
[64] Z.Q. Li, C.J. Lu, Z.P. Xia, Y. Zhou, Z. Luo, X-ray diffraction patterns of graphite and turbostratic carbon, Carbon 45 (2007) 1686–1695.
[65] S. Qiu, Y. Zhou, X. Zhou, T. Zhang, C. Wang, R.K.K. Yuen, W. Hu, Y. Hu, Air-stable polyphosphazene-functionalized few-layer black phosphorene for flame retardancy of epoxy resins, Small 15 (10) (2019) 1805175, https://doi.org/10.1002/smll.v15.1010.1002/smll.201805175.
[66] Q. Qi, P.L. Zheng, Y.J. Lei, X.B. Liu, Design of bi-modal pore structure polyarylene ether nitrile/$SiO_2$ foams with ultralow-k dielectric and wave transparent properties by supercritical carbon dioxide, Compos. Part B-Eng. 173 (2019), 106915.
[67] W. Zhang, X. Li, R. Yang, Pyrolysis and fire behaviour of epoxy resin composites based on a phosphorus-containing polyhedral oligomeric silsesquioxane (DOPO-POSS), Polym. Degrad. Stabil. 96 (2011) 1821–1832.